The Origin of Outflows in Evolved Stars
Proceedings IAU Symposium No. 366, 2022
L. Decin, A. Zijlstra & C. Gielen, eds.
doi:10.1017/S1743921322000187

Simulations of Colliding Winds in Massive Binary Systems with Accretion

Amit Kashi[1,2] **and Amir Michaelis**[1]

[1]Department of Physics, Ariel University, Ariel, 4070000, Israel

[2]Astrophysics Geophysics And Space Science Research Center (AGASS), Ariel University, Ariel, 4070000, Israel
e-mails: kashi@ariel.ac.il; amirmi@ariel.ac.il

Abstract. We run numerical simulations of massive colliding wind binaries, and quantify the accretion onto the secondary under different conditions. We set 3D simulation of a LBV–WR system and vary the LBV mass loss rate to obtain different values of wind momentum ratio η. We show that the mean accretion rate for stationary systems fits a power law $\dot{M}_{\rm acc} \propto \eta^{-1.6}$ for a wide range of η, until for extremely small η saturation in the accretion is reached. We find that the stronger the primary wind, the smaller the opening angle of the colliding wind structure (CWS), and compare it with previous analytical estimates. We demonstrate the efficiency of clumpy wind in penetrating the CWS and inducing smaller scale clumps that can be accreted. We propose that simulations of colliding winds can reveal more relations as the ones we found, and can be used to constrain stellar parameters.

Keywords. stars: massive — stars: mass-loss — stars: winds, outflows — (stars:) binaries: general — stars: Wolf-Rayet — accretion, accretion disks

1. Introduction

Massive stars have very intense winds, especially at late evolutionary stages (Langer 2012; Smith 2014; Owocki 2015; Vink 2015). These stars can undergo giant eruptions during which the mass loss rate is as high as a few $\rm M_\odot\ yr^{-1}$. Perhaps the most extreme example is the Great Eruption of η Carinae (e.g., Davidson & Humphreys 2012, and refs. therein), an interacting colliding wind systems with stellar masses that may reach 250 $\rm M_\odot$ (Kashi & Soker 2009a). The system had two extreme outbursts in the 17$^{\rm th}$ century known as the Great Eruption and Lesser Eruption, that caused the system to brighten and expelled as much as 40 $\rm M_\odot$ to form a bipolar nebula (e.g., Davidson & Humphreys 2012). Soker (2005) suggested that the Great Eruption was the result of mass accretion onto the secondary star, and that jets from an accretion disk around the secondary formed the bipolar nebula. Kashi & Soker (2009a) showed that using accretion and mass loss it is possible to account for the peaks in the light curve of the Great Eruption and Lesser Eruption, when assuming they occur near periastron passages. This might have altered the evolution of both stars (Kashi et al. 2016), implying that accretion can play an important role in the evolution and outcome of massive star binaries. The same scenario might have caused other giant eruptions, like the 17$^{\rm th}$ century eruptions of the prototype Luminous Blue Variable (LBV) star P Cygni (Kashi 2010; Michaelis et al. 2018).

Some massive binary systems can experience accretion not only during eruptions but also during quiescence times. Kashi (2019) showed that even for the present mass loss rate of the primary of η Car, which is in the order of $\sim 1/1000$ of the mass loss rate of the Great Eruption, accretion occurs close to periastron passage. An example for accretion in

younger massive binaries is the binary system HD 166734, studied in Kashi (2020). This system has an O7.5If primary and O9I(f) secondary with an orbital period of $\simeq 34.538$ days and eccentricity $\simeq 0.618$. The winds were highly unstable to the non-linear thin shell instability as they were radiative from both sides, creating long fingers instead of a smooth conical-like colliding wind structure (CWS). We obtained accretion for a long duration of the orbital period, that sums up to 1.3×10^{-8} $M_\odot$ each cycle. It is safe to assume that many more systems have stellar and orbital parameters that result in accretion, justifying a theoretical study of the problem.

Let us go back to the classical description of the colliding wind problem. When a massive binary system has two stars that both eject winds, the two winds collide and create a structure referred to as the CWS (Stevens et al. 1992; Usov 1992; Eichler & Usov 1993). In the most simple case, the CWS has two shocked winds separated by a contact discontinuity and curved into a conical like structure towards the star with the wind with the lower momentum. The symmetry line of the CWS in the absence of orbital motion is a line connecting the two stars. The shocked gas flows away asymptotically along the sides of the CWS towards infinity.

The main parameter that determines the shape of the contact discontinuity is the momentum ratio of the two winds

$$\eta = \frac{\dot{M}_2 v_2}{\dot{M}_1 v_1}, \tag{1.1}$$

where $\dot{M}_2$ and v_2 are the mass loss rate and the velocity of the wind of the secondary, and $\dot{M}_1$ and v_1 are the same for the primary. In the system we study here we will refer to the LBV as the primary and the WR as the secondary.

When orbital motion is added, the structure can take a conical-like shape or a spiral shape depending on the momentum ratio of the winds and the ratio between the winds velocity and the orbital velocity. At this point it is still possible to describe the system analytically, taking into account an approximation appropriate for the system and using toy-models. A well studied example is the model for η Carinae proposed in Kashi & Soker (2009b) that is based on a hyperboloid with a varying density that is rotated in a different angle at each point on an eccentric binary orbit depending on the orbital velocity and the stellar winds velocity vectors. This model was able to explain many of the observations of the system (Kashi & Soker 2007, 2008).

The next level of analysis in the attempt to understand colliding wind systems is to model them using numerical simulations. Modern simulations are performed in three dimensions and at high resolution that resolves fine details. They are composed of many ingredients and include relevant physical processes (e.g., Lamberts et al. 2011; Parkin et al. 2011; Parkin & Gosset 2011; Clementel et al. 2015; Hendrix et al. 2016; Reitberger et al. 2017; Kashi 2020; Kashi & Michaelis 2021). There is a wide space of uncertain parameters such that changing each one of them can cause observables of the CWS to change in a magnitude that is sometimes much larger than the rate of change the parameter had. An example for such a parameter is the eccentricity of the system, that is hard to constrain and can enormously change the results. To add to the complication, sometimes two different values of eccentricity can give results that are close enough indistinguishable by available observations (e.g., Davidson et al. 2017).

Though CWS have been simulated before, the first to obtain accretion were Akashi et al. (2013), who simulated η Carinae close to periastron passage. They found that dense clumps are formed by instabilities in the shocked primary wind as the winds collide. Those clumps flow towards the secondary but cannot be decelerated by the ram pressure of the secondary wind and hit the regions from where the secondary wind is launched. Our later simulations in Kashi (2017) included radiation pressure and showed

https://doi.org/10.1017/S1743921322000187 Published online by Cambridge University Press

that radiative breaking cannot prevent the accretion, by that confirming the theoretical prediction given by Kashi & Soker (2009c). These simulations in Kashi (2017) are also the first that solve the stars not as point sources but as approximated spheres, allowing directional analysis for accretion. In Kashi (2019) we studied four methods for treating accretion and the response of the accretor to the incoming wind, and found a numerical implementation for treating accretion and wind outflow simultaneously. We also showed that the accretion rate obtained when taking the secondary wind acceleration into account was higher than for ejecting winds at terminal speed.

While there are advanced numerical simulations studying colliding winds, most of them are focused on one specific binary system with its particular conditions (masses and radii of the stars, mass loss rates and velocities of the winds, orbital parameters, etc.). There is no set of *general* simulations that ran over a range of each of the parameters and isolated the influence of each physical effect. While obtaining such a set requires a very large number of observations, focusing on specific links between parameters through a limited set of simulations can also be very useful.

We discuss our recent set of colliding wind binaries simulations that cover part of the parameter space and focus on the shape of the colliding wind structure and accretion. Some of our results were presented in (Kashi & Michaelis 2021).

2. Accretion dependence on wind momentum ratio

We test the effect of an enhanced primary wind on the amount of accreted gas onto the primary. We neutralize the effect of orbital motion, in order to isolate the effect of the primary mass loss rate. The effect of enhancing the primary mass loss rate is equivalent to decreasing the momentum ratio.

We set up a stationary binary system with masses $M_1 = 80$ M$_\odot$ and $M_2 = 20$ M$_\odot$. For the fiducial run the primary mass loss rate is $\dot{M}_1 = 3 \times 10^{-4}$ M$_\odot$ yr^{-1} and its wind velocity has a terminal value of $v_{1,\infty} = 500$ km s^{-1} with radiative acceleration corresponding to $\beta = 1$. The secondary mass loss rate is $\dot{M}_2 = 10^{-5}$ M$_\odot$ yr^{-1}, and its wind velocity has a terminal value $v_{2,\infty} = 3000$ km s^{-1} with an acceleration parameter $\beta = 0.8$. We start the simulation with the two smooth winds (homogeneous without clumps). The momentum ratio is $\eta = \dot{M}_2 v_{2,\infty} / \dot{M}_1 v_{1,\infty} = 0.2$, but as the winds collide before reaching their terminal velocity, the effective momentum ratio is different and varies with location.

At $t = 68.5$ days the winds have filled most of the simulation volume and the CWS has reached a quasi-stable state. At this time we increase the mass loss rate of the primary to a larger value. The enhanced primary wind facing the secondary reaches the apex ≈ 14 days after its ejection. When it arrives to the colliding wind structure it disrupts its shape and induces stronger instabilities. The instabilities create dense fingers that penetrate the colliding wind structure and face the secondary.

We increase the primary mass loss rate, effectively reducing the momentum ratio η, and checking the amount of accreted mass on the companion as a result. The primary wind collides with the pre-existing CWS and changes its shape to a smaller opening angle. The side of the CWS facing the secondary shows strong instabilities and forms dense clumps and filaments. The gravity of the secondary pulls these filaments, and some of them are accreted onto the secondary. The secondary wind tries to flow against the incoming gas and forms bubbles.

We test a few values of the momentum ratio and find that for $\eta = 0.05$ accretion is first obtained. Figure 1 shows density slices with velocity vectors for six differnt times, as the enhanced primary wind propagates, interacts with the CWS and reshape it into a narrower structure. A 3D view is shown in Figure 2. We also calculate the X-ray emitted in the 2–10 KeV range (Figure 3). The emission shows a first large peak at the time the enhanced wind of the primary reaches the pre-existing colliding wind structure. After

https://doi.org/10.1017/S1743921322000187 Published online by Cambridge University Press

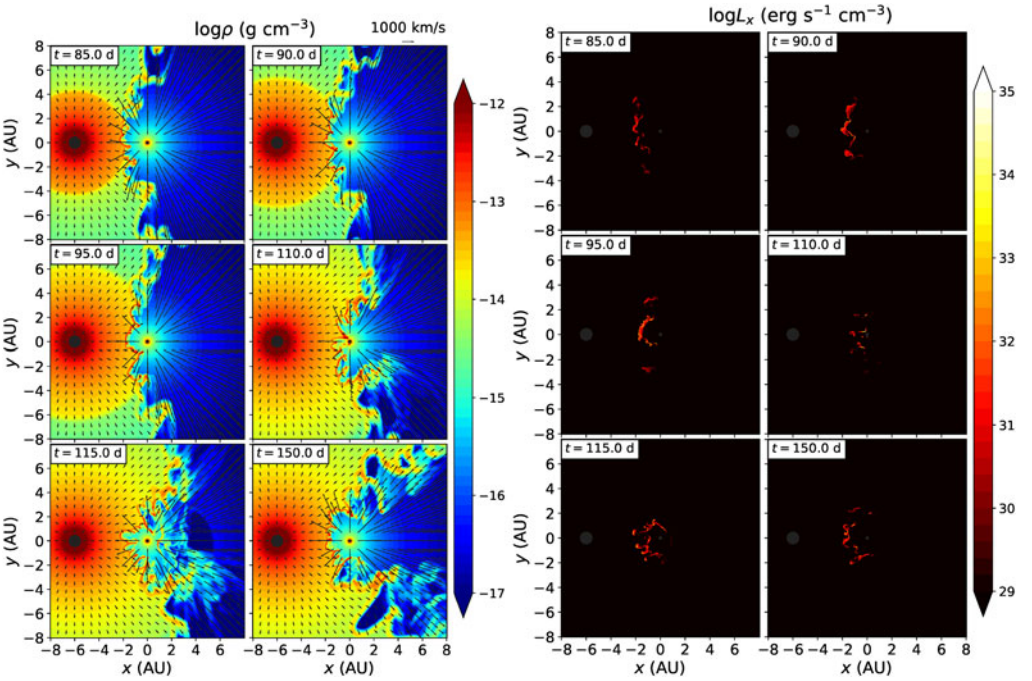

Figure 1. Left: Density maps with velocity vectors showing slices in the orbital plane ($z = 0$), for our simulation with $\eta = 0.05$. Right: X-ray emission at 2–10 KeV. Since the experiment is performed on stationary stars with no orbital motion, the slice of on the orbital plane is essentially similar to slice on any other plane around the axis joining the two stars. The secondary is at the center, marked with a small black circle while the primary, marked with a large blacked circle, is on the left side. The two winds are accelerated and collide. The primary then ejects an enhanced wind that interacts with the secondary wind at the CWS. For $\eta > 0.05$ we did not obtain accretion, however for this run clumps form the CWS penetrate into the secondary wind and accrete onto the secondary.

that, there is a quiescence level of emission, associated with the new meta-stable colliding wind structure. The actual observed X-ray flux from such a system will depend on the absorption in the line of sight, and is expected to look different from different directions. Figure 3 shows the mass accretion rate for our simulations for 400 days together with the 2–10 KeV emission. We find that the average mass accretion rate for $\eta = 0.05$ is $\dot{M}_{\rm acc,av} \simeq 1.7 \times 10^{-6}$ M$_\odot$ yr^{-1}. The accretion is intermittent, with irregular intervals and an average accretion duty cycle of $\simeq 0.055$.

We run more simulations with smaller values of η and calculate the acctetion rate onto the secondary for each of them. Figure 4 presents a simulation with mass loss rate of $\dot{M}_1 = 0.192$ M$_\odot$ yr^{-1}, and $\eta = 3.125 \times 10^{-4}$. This strong mass loss rate corresponds to a giant LBV eruption, and is an extreme case of colliding winds binary. For this simulation the secondary wind cannot blow against the strong primary wind, and is almost completely suppressed. The secondary accretes directly from the primary wind from all directions except a narrow solid angle at the side facing away from the primary. The secondary focuses the primary wind to create a narrow dense column behind the secondary, that has therefore higher density than other directions (Figure 5).

The X-ray emission curve has a strong peak when the enhanced primary wind interacts with the CWS and secondary wind, and later it is almost completely suppressed as the CWS does not exist any longer and the primary wind fills almost the entire volume, allowing only small region behind the secondary to emit.

https://doi.org/10.1017/S1743921322000187 Published online by Cambridge University Press

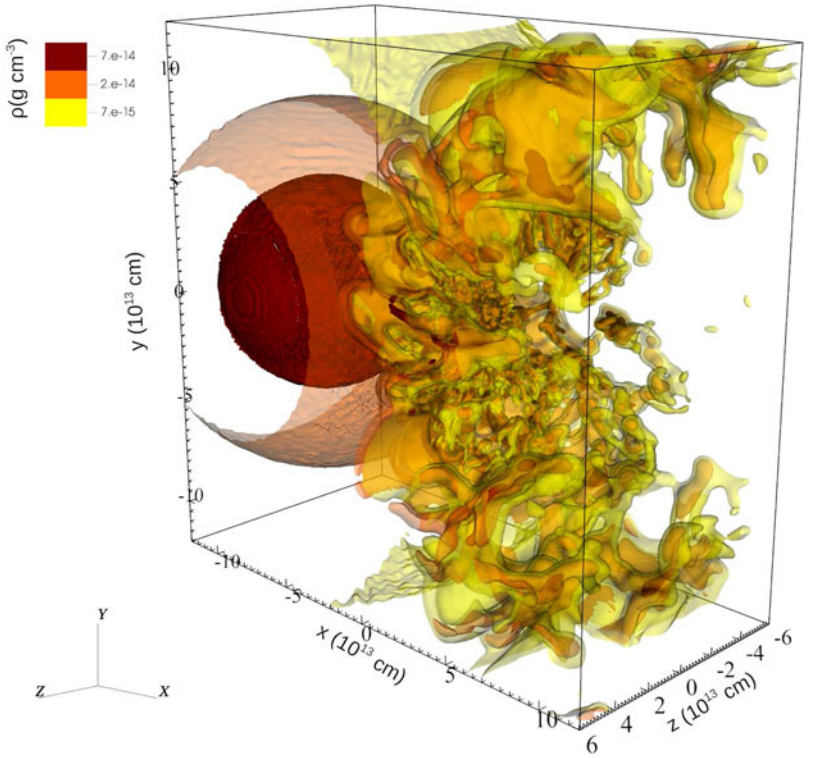

Figure 2. A three dimensional view of the colliding wind structure for $\eta = 0.05$. The stars are not shown. The view point is with the secondary closer to the observer. The primary is inside the red sphere in the far side of the figure (the sphere is a shell of the wind; not the stellar surface). The highly unstable structure of the colliding winds is revealed, with instabilities that created filaments and clumps. The flow is along the sides of the CWS, and the cavity is the secondary wind which has lower density and does not show in the image. At the point in time the figure shows there is no accretion but the CWS reaches very close to the secondary.

Figure 7 shows the average accretion rate in our simulations as a function of η. Simulations we ran with $\eta > 0.05$ did not yield any accretion and therefore do not show in the diagram as they have $\dot{M}_{\rm acc,av} = 0$. We can identify different regions in the $\dot{M}_{\rm acc,av}$–η diagram (Figure 7):

(i) No accretion: For $0.05 \lesssim \eta$ the secondary wind pushes away all the primary wind material, there is a well-defined CWS and no accretion ($\dot{M}_{\rm acc,av} = 0$).

(ii) Accretion: This region extends in the range $0.001 \lesssim \eta \lesssim 0.05$. For $0.02 \lesssim \eta \lesssim 0.05$ there is a transition region, in which accretion is very sporadic. Mass can occasionally be accreted but for most of the time the secondary wind and radiation prevent accretion. This is the region where radiative breaking is dominant. For $0.001 \lesssim \eta \lesssim 0.02$ accretion occurs most of the time. The accretion rate and the accretion duty cycle are larger as η decreases. We fit the simulations' results in region (ii) and find a power-law relation that satisfies

$$\dot{M}_{\rm acc,av} \propto \eta^{-1.6}. \tag{2.1}$$

(iii) Saturated accretion: For $\eta \lesssim 0.00125$ the accretion becomes continuous in time and the accretion rate is constant. The value of $\dot{M}_{\rm acc,av}$ approaches saturation as η continues to decrease. For $\eta \lesssim 0.0003125$ there is saturation in the accretion at $\dot{M}_{\rm acc,sat} \approx 3 \times 10^{-3}$ M$_\odot$ yr^{-1}.

https://doi.org/10.1017/S1743921322000187 Published online by Cambridge University Press

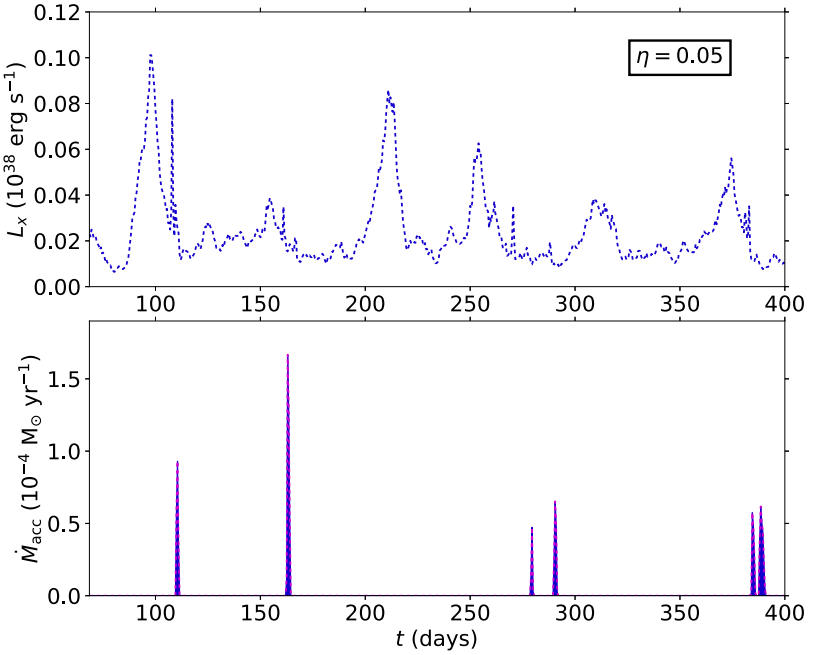

Figure 3. Lower panel: Resulted mass accretion rate onto the secondary for the simulation with $\eta = 0.05$, the highest value of η for which accretion was obtained. Accretion only happened in brief episodes that last ≈ 2 days where a clump is being accreted. In between episodes there are long duration with no accretion. ($\eta = 0.05$) Upper panel: X-ray emission at 2–10 KeV integrated over the simulations volume.

The very low values of η in region (iii) do not describe the colliding wind problem in the sense that there are no two colliding winds with post-shocked gas, and not a CWS as for larger η. Instead, there is only a small region behind the secondary where X-ray is emitted from the heated primary wind that collides with itself after being focused by the secondary, as seen in Figure 4. Our results for the very low values of η, correspond a strong mass loss rate from the LBV, as occurs during giant eruptions.

3. The opening angle for low momentum ratio

The semi-opening angle of the CWS can be obtained by solving a non-linear differential equation for the momentum ratio η. It was calculated numerically by Girard & Willson (1987), and for intermediate values of η there is an approximation derived by Eichler & Usov (1993):

$$\theta \approx 2.1 \left(1 - \frac{\eta^{2/5}}{4}\right) \eta^{1/3}, \tag{3.1}$$

which is stated to be accurate to about 1%. The expression for the shape of the CWS was later revisited a number of times (e.g., Gayley 2009; Pittard & Dawson 2018).

In fact, the actual shape of the CWS is more complicated, taking other factors into account. Among the factors we can count:

- The value of η is location dependent, due to the acceleration of the wind that results in the winds meeting at different velocities than terminal.
- Clumps in the winds (small-scale inhomogeneities common in winds of massive stars; e.g., Crowther et al. 2002; Walder & Folini 2002; Moffat 2008) flow and interact with the other wind resulting the CWS to be inhomogeneous.

https://doi.org/10.1017/S1743921322000187 Published online by Cambridge University Press

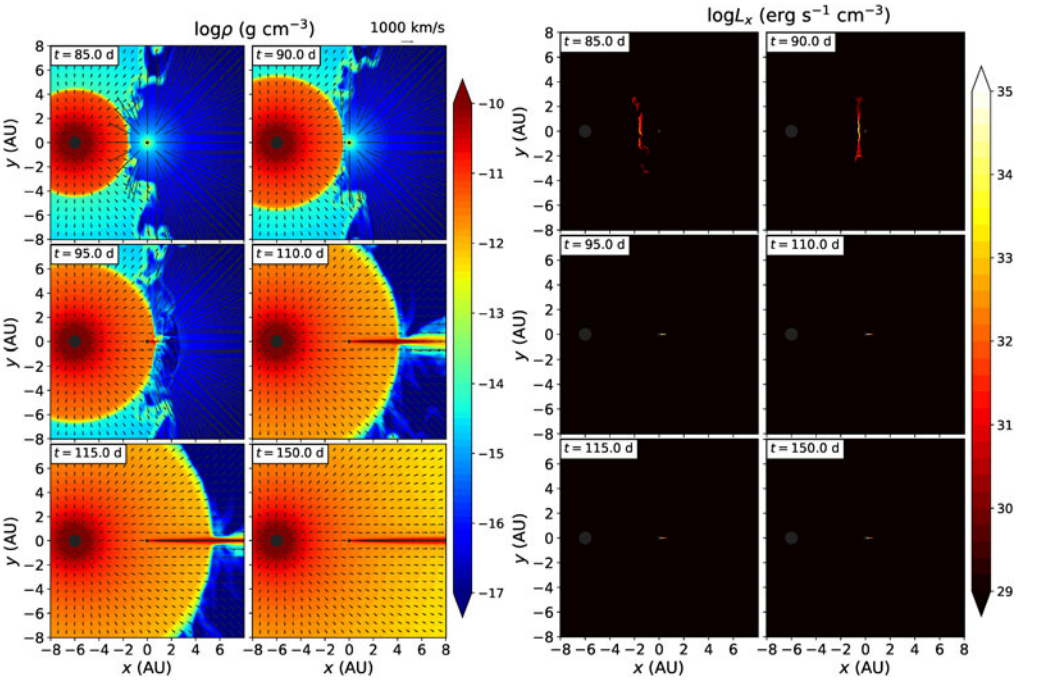

Figure 4. Same as Figure 1, but for $\eta = 3.125 \times 10^{-4}$. The secondary accretes directly from the primary wind from all directions except a narrow solid angle at the side facing away from the primary. The secondary focuses the primary wind to create a narrow dense column behind the secondary. X-ray is emitted from a very small region behind the secondary.

• Instabilities arise when the winds collide, as a result of cooling that will form clumps in the colliding wind region.

• The radiation field of the secondary (the star with the weaker wind) may decelerate the primary incoming wind (radiative inhibition; Owocki & Gayley 1995; Gayley et al. 1997).

• Mixing can result in a range of flow speeds instead of a single uniform one (e.g., Gayley 2009).

• Orbital motion completely alters the CWS shape, making it rotate and wind around itself and casing aberration. Moreover, in eccentric orbits the distance between the stars and the orbital velocity is time dependent, causing periodic changes in the CWS.

We take our simulations of static colliding winds, mostly focusing on low values of the momentum ratio (highly uneven winds that have accretion), and calculate the semi-opening angle for them. The formation of instabilities makes the shape of the winds complicated and a fitting process is needed. We use image processing methods to fit the shape line of the wind, an imaginary line dividing the turbulent flow into two domains, and the semi-opening angle. Then, based on the shape of the wind and the location of the primary and secondary, we can derive the semi-opening angle of the wind. Figure 8 shows the resulting opening angle for our for three different cases.

We plot the wind semi-opening angle as a function of η in Figure 9. For most of our simulations, the simulations obtain larger opening angles than Equation (3.1). For $\eta \lesssim 2 \times 10^{-3}$, we obtain a smaller semi-opening angle than the result from equation (3.1). The equation is actually not applicable for such a small value of η. In this run, the strong mass loss from the primary chokes the secondary wind almost completely. Therefore, the semi-opening angle does not really describe the same problem of colliding winds of two

https://doi.org/10.1017/S1743921322000187 Published online by Cambridge University Press

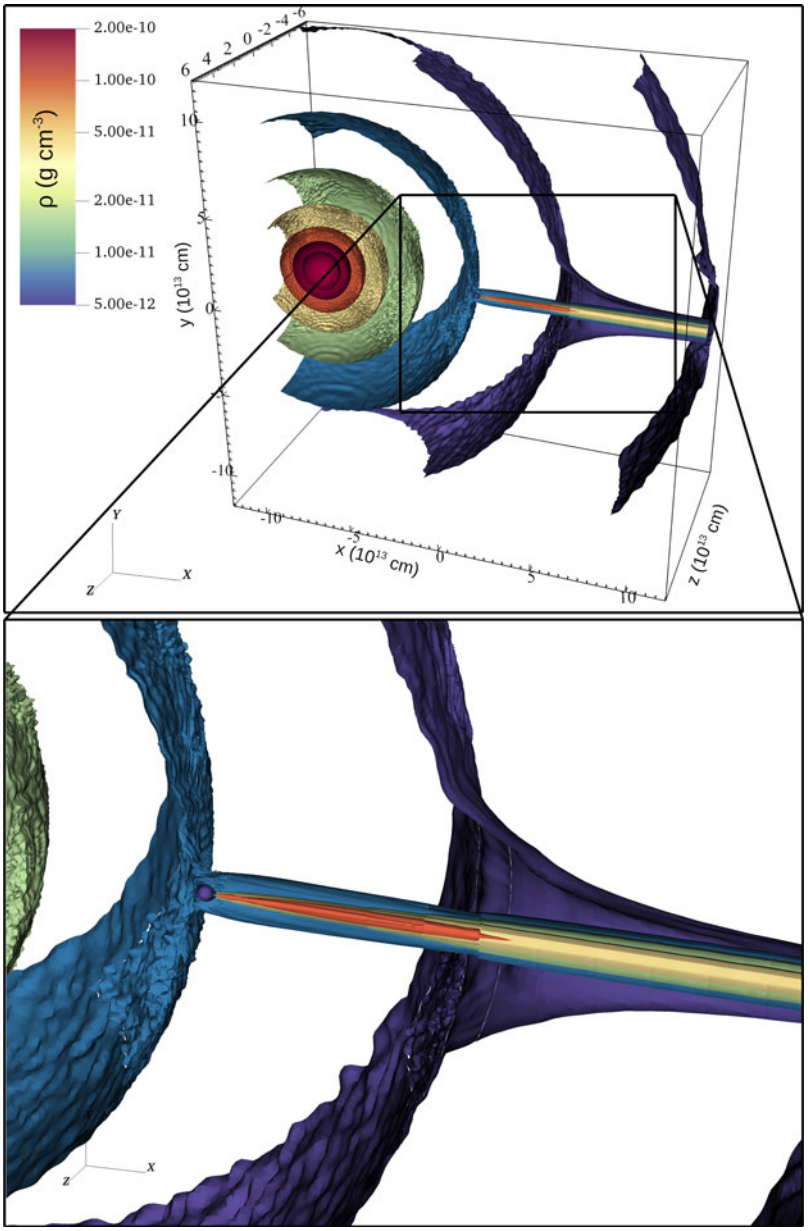

Figure 5. A three dimensional view of the colliding wind structure for $\eta = 3.125 \times 10^{-4}$. The secondary wind is almost completely suppressed. Accretion arrives from the side facing the primary. The secondary focuses the primary wind into a dense column behind the secondary.

stars, but rather the collision of the primary wind with itself after being focused by the secondary and its gravitational field.

4. Clumpy Wind and accretion

Evolved massive stars generally have isotropic winds on a large scale. Wind-clumping refers to small-scale density inhomogeneities distributed across the wind. The clumps have a much larger optical thickness than the gas among the clumps. Because clumping

https://doi.org/10.1017/S1743921322000187 Published online by Cambridge University Press

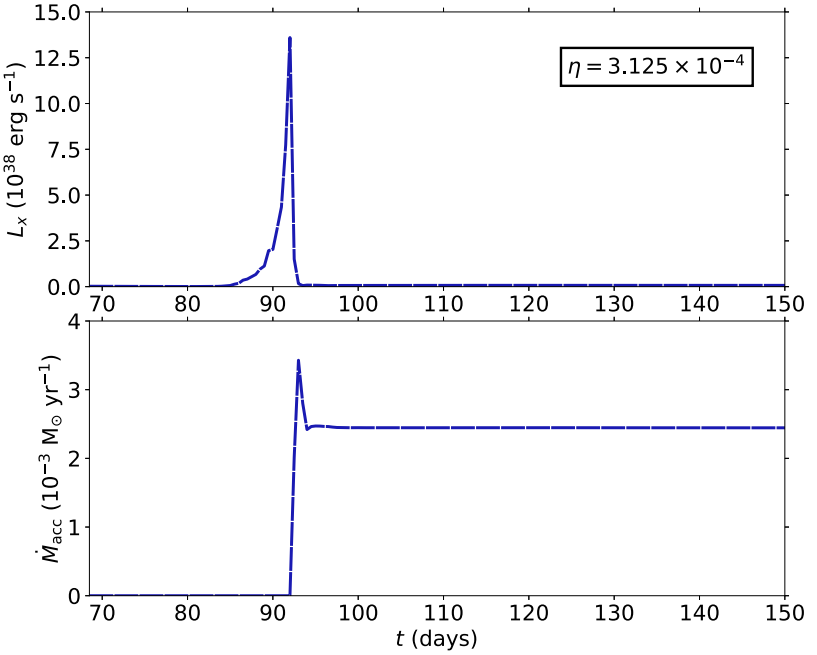

Figure 6. Lower panel: Resulted mass accretion rate onto the secondary for the simulation with $\eta = 3.125 \times 10^{-4}$. At this very high primary mass loss rate accretion occurs continuously. Upper panel: X-ray emission at 2–10 KeV integrated over the simulations volume.

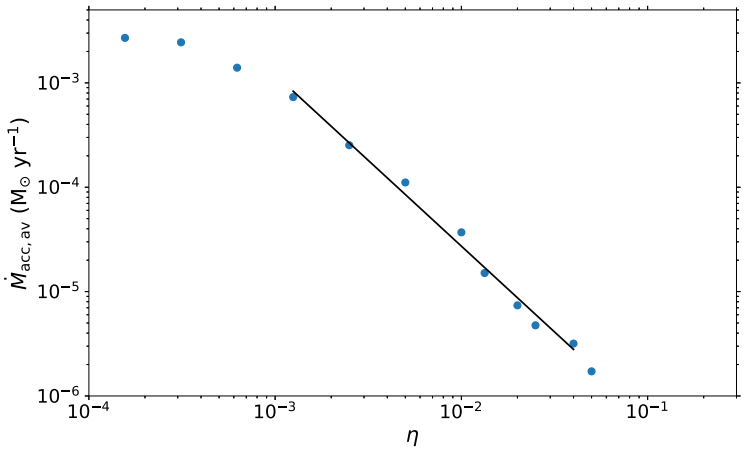

Figure 7. The $\dot{M}_{\rm acc} - \eta$ diagram. The accretion rate obtained from our simulations. Simulations with $\eta > 0.05$ did not yield any accretion. There are different regions in the figure (see text). The straight line indicated the power law described in equation (2.1) For lower η there is transition into saturation value in the mass accretion rate.

contaminates diagnostics that are based on mass-loss, it might result in reduction of previously derived mass-loss rates for massive star (Puls et al. 2008). The effect of wind clumping on mass loss rate is non negligible. For Wolf-Rayet (WR) stars, the realization that their winds are clumped lead to a decrease in the mass-loss rate by a factor 2–4 (e.g., Moffat & Robert 1994; Hamann & Koesterke 1998; Nugis & Lamers 2000). More recent works suggest that the clumping factor is larger $\simeq 10$ (Hainich et al. 2014; Shenar et al. 2019).

https://doi.org/10.1017/S1743921322000187 Published online by Cambridge University Press

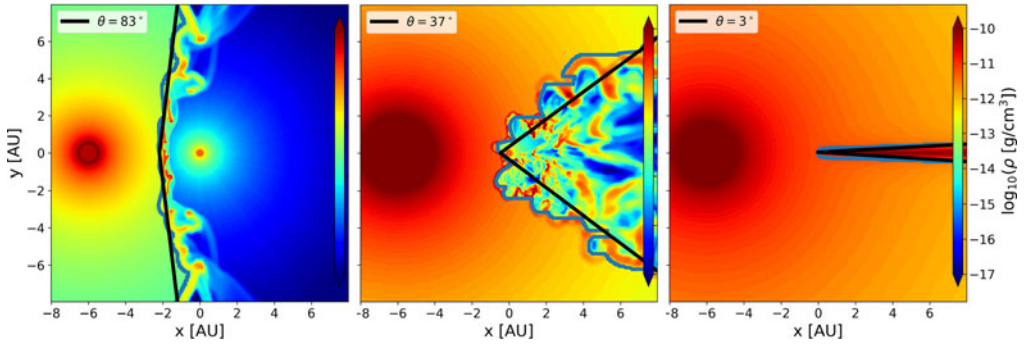

Figure 8. A fit to the colliding wind structure semi-opening angle. The blue line is the result of the wind shape detection algorithm and the black line is the optimal line of the asymptotic opening. Left: $\eta = 0.2$; Middle: $\eta = 0.01$; Right: $\eta = 1.5625 \times 10^{-4}$.

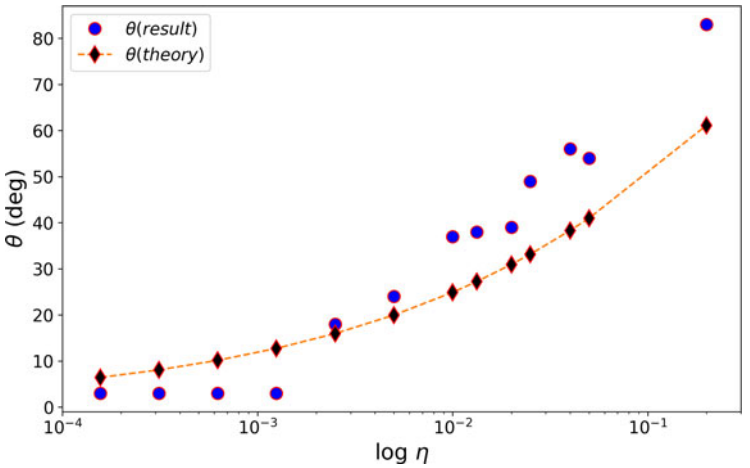

Figure 9. Wind semi-opening angle at time $t = 150$ days. We include the theoretical value according to Equation (3.1) (marked 'theory'; red diamonds) and the simulations' results (blue circles).

Recently, Zhekov (2021) studied X-ray observations of the prototype colliding wind binary WR 140, and found that a standard colliding wind model with smooth winds does not match the X-ray line profiles. They suggested that adding clumps to the WR wind can solve the discrepancy, and concluded that the clumps are efficiently dissolved in the colliding wind region when the stars are near apastron but not at periastron (the system is highly eccentric $e \approx 0.9$).

We run a simulation with a similar setting to the simulation with $\eta = 0.2$ as in section 2, but this time instead of enhancing the wind in an isotropic way we make a a sudden ejection of clumps. The degree of clumping can be measured by the clumping factor $f_{\rm cl} = \langle \rho^2 \rangle \, / \, \langle \rho \rangle^2$, where ρ is the density of the wind. The clumps are ejected symmetrically evenly spaced in volume. Obviously clumps can be ejected continuously, and at different densities and sizes. We here examine a simple setting of spherically distributed clumps. We take very large clumps that are larger than what one would expect to see in a realistic system. The symmetrical ejection of clumps in our experiment is in agreement with the findings of Gootkin et al. (2020) who found that clumps are evenly distributed around the prototype LBV star P Cygni. The clumps are ejected from a region very close to the star $\simeq 1.1 R_1$, in agreement with the results of Sundqvist & Owocki (2013).

https://doi.org/10.1017/S1743921322000187 Published online by Cambridge University Press

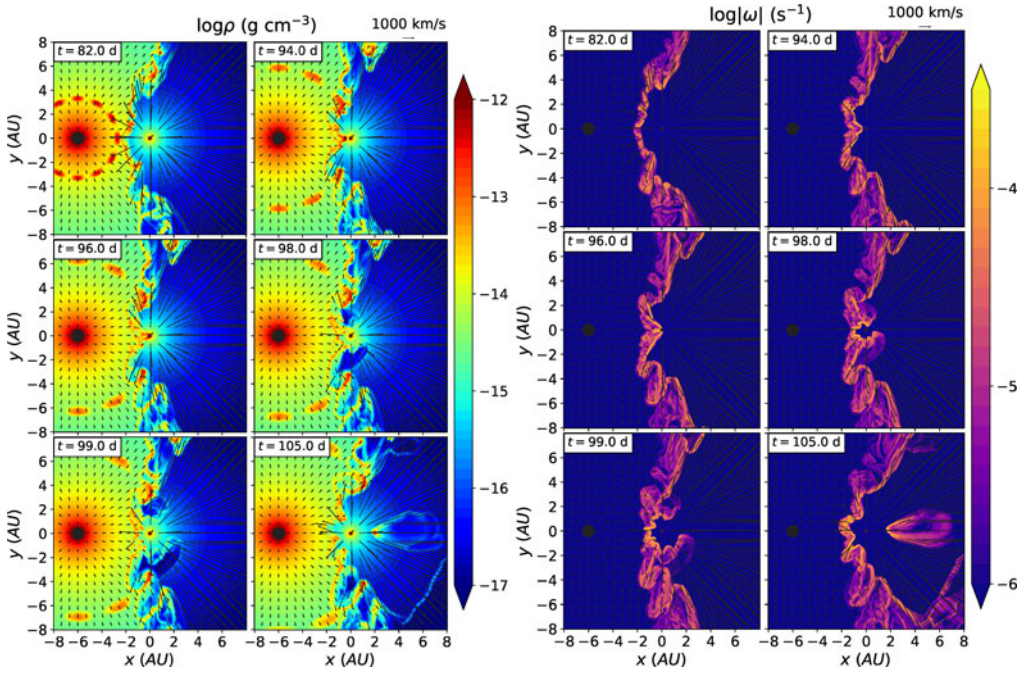

Figure 10. Clumps launching simulation with clumping factor $f_{\rm cl} = 1.66$. Left: Density maps with velocity vectors showing slices in the orbital plane ($z = 0$). The primary wind ejects clumps that interact with the secondary wind at the colliding wind region, and then penetrate into the secondary wind and accrete onto the secondary. At later times a dense clump is formed on the right side of the secondary. Right: The absolute value of the vorticity, as calculated from equation 4.1.

The clumps propagate radially, expend, and their density decreases. The clumps reach the colliding wind structure gradually, first the apex (the line connecting the primary and the secondary), and further regions at later times. The instabilities create dense fingers that penetrate the colliding wind structure and face the secondary. The secondary gravity then pulls the fingers, and the secondary wind pushes it away. Depending on the dominant force, the clump might get accreted. In our simulation with where the clumps overdensity was large enough, the clumps did penetrate the secondary wind and gas was accreted onto the secondary.

If the clumps density is not large enough, we find that the launched clumps dissipate by the time they reach the CWS and have a very small effect that can be quantified as reducing the momentum ratio η (equation 1.1). We then ran an experiment with clump densities of 20 times the density of the smooth wind, which corresponds to a larger clumping factor $f_{\rm cl} = 1.66$. The left panel of Figure 10 shows density maps for the simulation in the orbital plane ($z = 0$), at different times of the simulation.

We process our simulations' results to derive hydrodynamical quantities that can serve as indicators to the effect of the clumps on the colliding wind structure and the vicinity of the secondary, and allow us to quantify the effect of clump interaction.

For each point in our grid we calculate the vorticity, which measures the local rotation of a fluid parcel

$$\omega = \nabla \times \mathbf{v}. \tag{4.1}$$

https://doi.org/10.1017/S1743921322000187 Published online by Cambridge University Press

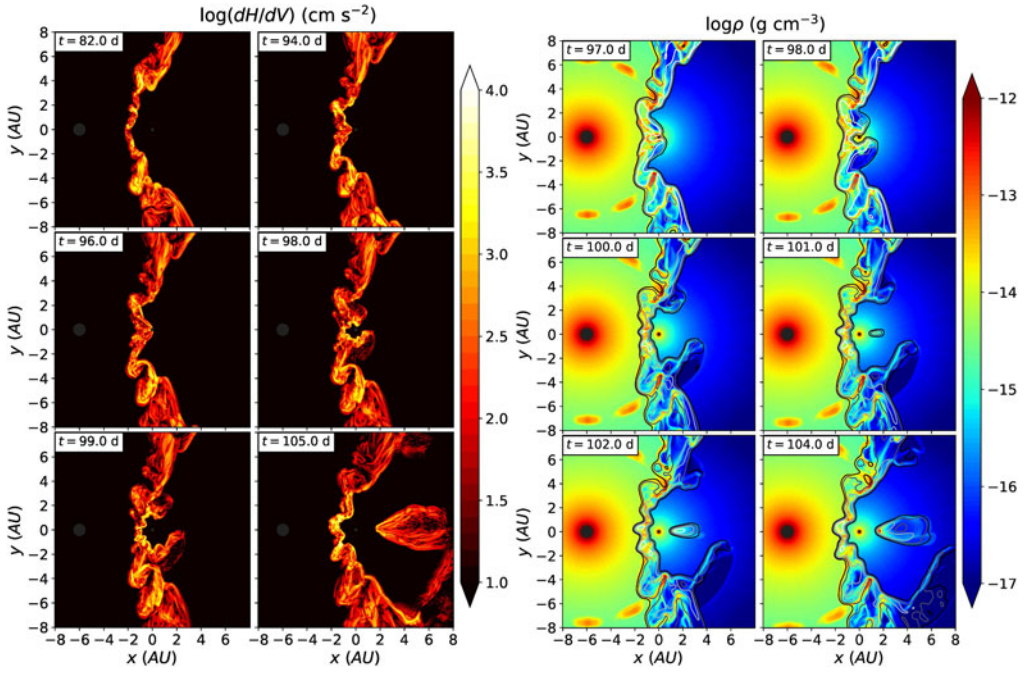

Figure 11. Left: Maps showing the specific helicity (helicity per unit volume) of the flow on the orbital plane. At later times, after the clumps had penetrated the colliding wind structure and some of the mass was accreted the downstream clumps are formed. Right: Density map together with vorticity contours showing the accretion phase ($t = 97$ days) and the following formation of the downstream blob. Vorticity contours (for the norm value) are smoothed using Gaussian smoothing and range from 10^{-6} s^{-1} (black) to 10^{-3} s^{-1} (white).

In the right pane of Figure 10 we show the absolute value of the vorticity ω. The helicity is a quantity that measures the degree of knottedness in the vortices (Moffatt 1969), defined as

$$H = \int_V \mathbf{v} \cdot (\nabla \times \mathbf{v})\, dV. \tag{4.2}$$

The integral over volume gives indication to the turbulence of the flow in that volume. The specific helicity, namely the helicity per unit volume is

$$\frac{dH}{dV} = \mathbf{v} \cdot (\nabla \times \mathbf{v}). \tag{4.3}$$

The left panel of Figure 11 shows maps of the helicity, at times similar to those in Figure 10. The vorticity and helicity maps emphasize every part of the hydrodynamical volume that does not flow in a laminar way (note that the ejected clumps are not seen until they interact with the CWS). This allows a quantitative measurement of the instabilities in the CWS, as well as detection of clumped regions.

We find that the amount of mass accreted onto the secondary is $M_{\rm acc} \simeq 3.3 \times 10^{-7}$ M$_\odot$. This amount of mass is accreted over a short period of only $\simeq 2$ days. The total energy is $\simeq 5 \times 10^{41}$ erg and the average power is $\simeq 2.9 \times 10^{36}$ erg s^{-1}. After the clumps have passed the colliding wind structure and some of the gas was accreted onto the secondary, the secondary wind has cleared the volume around the star and the secondary wind flow has been restored. However, on $t \simeq 105$ days the density map shows a massive clump that has formed on the side of the secondary opposite to the primary and the apex of the colliding wind structure. This downstream clump contains $\approx 10^{23}$ g , with a peak

https://doi.org/10.1017/S1743921322000187 Published online by Cambridge University Press

density of $\simeq 5 \times 10^{-13}$ g cm^{-3} and is being pushed away by the secondary wind (towards positive x axis). The density map does not easily reveal why this massive clump formed. The vorticity map and helicity map provide a hint. As seen in Figure 11 the region around the secondary became very turbulent after the accretion. This turbulence might have induced the formation of the massive downstream clump. The helicity and vorticiy maps show that a large volume is turbulent. Part of this region collapses to form the downstream clump.

5. Summary

We describe numerical experiments of a colliding wind LBV–WR system under momentum ratio η (equation 1.1). We run a set of simulations and measure the amount of mass accreted onto the secondary star and its X-ray emission. The instabilities in the CWS have the velocity component in the direction of the flow (namely, along the sides of the CWS) but also have the acceleration of the secondary. Depending on the parameters, some of the clumps can be pulled towards the secondary and get accreted. We find that above $\eta = 0.05$ there is no accretion. For smaller values the mass accretion rate follows a power law (equation 2.1), and the duty cycle of accretion becomes larger as η decreases. For $\eta \lesssim 0.001$ the accretion becomes continuous in time and the accretion rate is constant, and for $\eta \lesssim 0.0003$ there is saturation in the accretion rate, as the accretion is directly onto the secondary as there is no colliding wind structure.

The semi-opening angle for the CWS with instabilities is more complicated to define than for an adiabatic wind. We employ a numerical method to quantify it and find that it differs from the commonly used theoretical expression (equation 3.1) and for very low η it saturates (Figure 9). Our numerical method for extracting the wind angle has two major parameters: the degree of density change in the collusion region and the degree of smoothness after extracting the wind edge. We found that on most runs the parameters are very robust and changing them will result in the same angle, that gives us confidence in the method.

We showed an additional experiment in which clumps are ejected from the primary, travel towards the secondary and collide with the CWS. The interaction causes it to become unstable and form smaller clumps that are accreted onto the secondary. We demonstrated how the vorticity and helicity can be useful in quantifying the turbulent regions in the simulation, and propose they can be used for more diagnostics of the CWS and accretion.

The method demonstrated here – systematic exploration of the parameter space of massive colliding wind binaries – has shown to give quantitative relations between measurable parameters. There are many more parameters to cover, and probably more hidden relations. The observational signature of colliding wind systems spans across the spectrum. The simulations' results can be connected to observations of particular massive colliding wind binary systems, and be used to more tightly constrain stellar parameters. We therefore believe that such analysis of simulations of colliding wind binaries can be a useful tool in the study of massive stars and their evolution. This, in turn, has applications to our understanding how massive stars influence their galaxies through stellar winds, ionizing radiation, giant eruptions and supernovae explosions.

We acknowledge support from the R&D authority in Ariel University. We acknowledge the Ariel HPC Center at Ariel University for providing computing resources that have contributed to the research results reported within this paper.

References

Akashi, M. S., Kashi, A., & Soker, N. 2013, NewA, 18, 23, doi: 10.1016/j.newast.2012.05.010

Clementel, N., Madura, T. I., Kruip, C. J. H., & Paardekooper, J. P. 2015, MNRAS, 450, 1388, doi: 10.1093/mnras/stv696

Crowther, P. A., Dessart, L., Hillier, D. J., Abbott, J. B., & Fullerton, A. W. 2002, A&A, 392, 653, doi: 10.1051/0004-6361:20020941

Davidson, K., & Humphreys, R. M. 2012, 384, doi: 10.1007/978-1-4614-2275-4

Davidson, K., Ishibashi, K., & Martin, J. C. 2017, Research Notes of the American Astronomical Society, 1, 6, doi: 10.3847/2515-5172/aa96b3

Eichler, D., & Usov, V. 1993, ApJ, 402, 271, doi: 10.1086/172130

Gayley, K. G. 2009, ApJ, 703, 89, doi: 10.1088/0004-637X/703/1/89

Gayley, K. G., Owocki, S. P., & Cranmer, S. R. 1997, ApJ, 475, 786, doi: 10.1086/303573

Girard, T., & Willson, L. A. 1987, A&A, 183, 247

Gootkin, K., Dorn-Wallenstein, T., Lomax, J. R., et al. 2020, ApJ, 900, 162, doi: 10.3847/1538-4357/abad32

Hainich, R., Rühling, U., Todt, H., et al. 2014, A&A, 565, A27, doi: 10.1051/0004-6361/201322696

Hamann, W. R., & Koesterke, L. 1998, A&A, 335, 1003

Hendrix, T., Keppens, R., van Marle, A. J., et al. 2016, MNRAS, 460, 3975, doi: 10.1093/mnras/stw1289

Kashi, A. 2010, MNRAS, 405, 1924, doi: 10.1111/j.1365-2966.2010.16582.x

—. 2017, MNRAS, 464, 775, doi: 10.1093/mnras/stw2303

—. 2019, MNRAS, 486, 926, doi: 10.1093/mnras/stz837

—. 2020, MNRAS, 492, 5261, doi: 10.1093/mnras/staa203

Kashi, A., Davidson, K., & Humphreys, R. M. 2016, ApJ, 817, 66, doi: 10.3847/0004-637X/817/1/66

Kashi, A., & Michaelis, A. 2021, Galaxies, 10, 4, doi: 10.3390/galaxies10010004

Kashi, A., & Soker, N. 2007, MNRAS, 378, 1609, doi: 10.1111/j.1365-2966.2007.11908.x

—. 2008, NewA, 13, 569, doi: 10.1016/j.newast.2008.03.003

—. 2009a, NewA, 14, 11, doi: 10.1016/j.newast.2008.04.003

—. 2009b, MNRAS, 394, 923, doi: 10.1111/j.1365-2966.2008.14331.x

—. 2009c, NewA, 14, 11, doi: 10.1016/j.newast.2008.04.003

Lamberts, A., Fromang, S., & Dubus, G. 2011, MNRAS, 418, 2618, doi: 10.1111/j.1365-2966.2011.19653.x

Langer, N. 2012, ARA&A, 50, 107, doi: 10.1146/annurev-astro-081811-125534

Michaelis, A. M., Kashi, A., & Kochiashvili, N. 2018, NewA, 65, 29, doi: 10.1016/j.newast.2018.06.001

Moffat, A. F. J. 2008, in Clumping in Hot-Star Winds, ed. W.-R. Hamann, A. Feldmeier, & L. M. Oskinova, 17

Moffat, A. F. J., & Robert, C. 1994, ApJ, 421, 310, doi: 10.1086/173648

Moffatt, H. K. 1969, Journal of Fluid Mechanics, 35, 117, doi: 10.1017/S0022112069000991

Nugis, T., & Lamers, H. J. G. L. M. 2000, A&A, 360, 227

Owocki, S. P. 2015, in Astrophysics and Space Science Library, Vol. 412, Very Massive Stars in the Local Universe, ed. J. S. Vink, 113

Owocki, S. P., & Gayley, K. G. 1995, ApJL, 454, L145, doi: 10.1086/309786

Parkin, E. R., & Gosset, E. 2011, A&A, 530, A119, doi: 10.1051/0004-6361/201016125

Parkin, E. R., Pittard, J. M., Corcoran, M. F., & Hamaguchi, K. 2011, ApJ, 726, 105, doi: 10.1088/0004-637X/726/2/105

Pittard, J. M., & Dawson, B. 2018, MNRAS, 477, 5640, doi: 10.1093/mnras/sty1025

Puls, J., Vink, J. S., & Najarro, F. 2008, AAPR, 16, 209, doi: 10.1007/s00159-008-0015-8

Reitberger, K., Kissmann, R., Reimer, A., & Reimer, O. 2017, ApJ, 847, 40, doi: 10.3847/1538-4357/aa876d

Shenar, T., Sablowski, D. P., Hainich, R., et al. 2019, A&A, 627, A151, doi: 10.1051/0004-6361/201935684

Smith, N. 2014, ARA&A, 52, 487, doi: 10.1146/annurev-astro-081913-040025
Soker, N. 2005, ApJ, 635, 540, doi: 10.1086/497389
Stevens, I. R., Blondin, J. M., & Pollock, A. M. T. 1992, ApJ, 386, 265, doi: 10.1086/171013
Sundqvist, J. O., & Owocki, S. P. 2013, MNRAS, 428, 1837, doi: 10.1093/mnras/sts165
Usov, V. V. 1992, ApJ, 389, 635, doi: 10.1086/171236
Vink, J. S. 2015, in Astrophysics and Space Science Library, Vol. 412, Very Massive Stars in the Local Universe, ed. J. S. Vink, 77
Walder, R., & Folini, D. 2002, in Astronomical Society of the Pacific Conference Series, Vol. 260, Interacting Winds from Massive Stars, ed. A. F. J. Moffat & N. St-Louis, 595
Zhekov, S. A. 2021, MNRAS, 500, 4837, doi: 10.1093/mnras/staa3591